Journal of Solid State Chemistry **143,** 122–131 (1999)
Article ID jssc.1998.8096, available online at http://www.idealibrary.com on IDEAL®

Modulated Structures in Oxidized Cerium Niobates

John G. Thompson and Ray L. Withers

Research School of Chemistry, Australian National University, Canberra, ACT 0200, Australia

and

Frank J. Brink

Electron Microscopy Unit, Australian National University, Canberra, ACT 0200, Australia

Received October 6, 1998; accepted November 3, 1998

Three previously reported oxidized cerium niobate phases $CeNbO_{4+x}$ ($x = 0.08$, 0.25, and 0.33) have been synthesized and characterized by X-ray powder and electron diffraction. All three phases display structures which are modulated variants of a parent fergusonite-type $Ce^{III}NbO_4$ structure (*I*2/*a*, $a = 5.5342(2)$ Å $b = 11.4016(6)$ Å, $c = 5.1583(3)$ Å, $\beta = 94.600(5)^\circ$). The $x = 0.08$ phase with parent unit cell (*I*2/*a*, $a = 5.3029(8)$ Å, $b = 11.483(2)$ Å, $c = 5.2515(8)$ Å, $\beta = 91.32(2)^\circ$) is a two-dimensional, incommensurately modulated phase characterized by incommensurate primary modulation wavevectors $\mathbf{q}_1 \sim [0.345, 0, 0.138]^*_p$ and $\mathbf{q}_2 \sim [-0.069, 0, 0.172]^*_p$ (p for parent). The $x = 0.25$ phase with parent unit cell (*I*2/*a*, $a = 5.3522(8)$ Å, $b = 11.374(3)$ Å, $c = 5.116(1)$ Å, $\beta = 93.34(2)^\circ$) is a commensurately modulated superstructure phase characterized by the reciprocal space unit cell $\mathbf{a}^*_r = \frac{1}{12}[402]^*_p$, $\mathbf{b}^*_r = \frac{1}{4}[020]^*_p$, and $\mathbf{c}^*_r = \frac{1}{3}[\bar{1}01]^*_p$ (r for resultant). The $x = 0.33$ phase with parent unit cell (*I*1, $a = 5.4374(8)$ Å, $b = 11.189(2)$ Å, $c = 5.1458(8)$ Å, $\alpha = 90.56(1)$, $\beta = 94.37(1)$, $\gamma = 88.19(1)^\circ$) is again commensurately modulated with $\mathbf{q} = \frac{1}{3}[101]^*_p$. The close structural relationship between the three oxidized phases and possible interstitial oxygen sites in the $Ce^{III}NbO_4$ structure are discussed. © 1999 Academic Press

INTRODUCTION

$CeNbO_4$ at room temperature has a monoclinic fergusonite-type structure (Fig. 1) which has been refined using neutron powder diffraction (1). When heated in vacuum $CeNbO_4$ undergoes a reversible displacive phase transition at 574°C to a tetragonal scheelite structure (2).

When $CeNbO_4$ is heated in air or oxygen, however, it is readily oxidized to yield several different phases, depending on the heating regime, according to the reaction $Ce^{III}NbO_4 + x\frac{1}{2}O_2 \rightarrow Ce^{III}_{1-2x}Ce^{IV}_{2x}NbO_{4+x}$. These oxidized phases were the subject of a series of combined TGA and X-ray diffraction (XRD; powder and single crystal) studies in the 1970s (3–6). Taken together these studies reported three distinct phases.

(i) A solid-solution phase with composition $0.06 \leq x \leq 0.12$ is observed when $CeNbO_4$ is heated in air above the monoclinic-tetragonal phase transition between 600 and 675°C for a limited time then rapidly quenched to room temperature (4).

(ii) A line phase of composition $x = 0.25$ is prepared when $CeNbO_4$ is heated in air at 600°C for at least 2.5 h (3). TGA measurements for this phase gave $0.243 \leq x \leq 0.254$ (3), consistent with a line phase, within experimental error.

(iii) A line phase of composition $x = 0.33$ is prepared when $CeNbO_4$ is heated in oxygen at 400°C for 24 h (5). The same phase can be prepared in air between 300 and 350°C given long annealing times and many intermediate regrindings.

Based on TGA observations Roth *et al.* (5) also mentioned the possibility of either a fourth oxidized phase between $x = 0.25$ and 0.33 or a solid-solution range for the $x = 0.25$ phase, though no further evidence for this has since been reported.

Cava *et al.* (6) reported that when the $x = 0.25$ phase is heated in air it is reduced to the $x \approx 0.08$ phase at 618 ± 4°C and is further reduced to $CeNbO_4$ at 642 ± 7°C. Negas *et al.* (1) showed that while $CeNbO_4$ was stable above 850°C, when heated for significant times between 750 and 850°C it was susceptible to oxidation/decomposition reactions, the details of which are contained in that reference.

By inspection of the X-ray powder diffraction data for the $x \approx 0.08$ and $x = 0.25$ phases the previous authors (3, 4) identified the close relationship between their structures and the fergusonite-type structure of the reduced phase $CeNbO_4$ and were able to fit their data to *I*-centered monoclinic unit cells (4). Precession photographs taken from single crystals of these two phases showed them both to have strong

0022-4596/99 $30.00

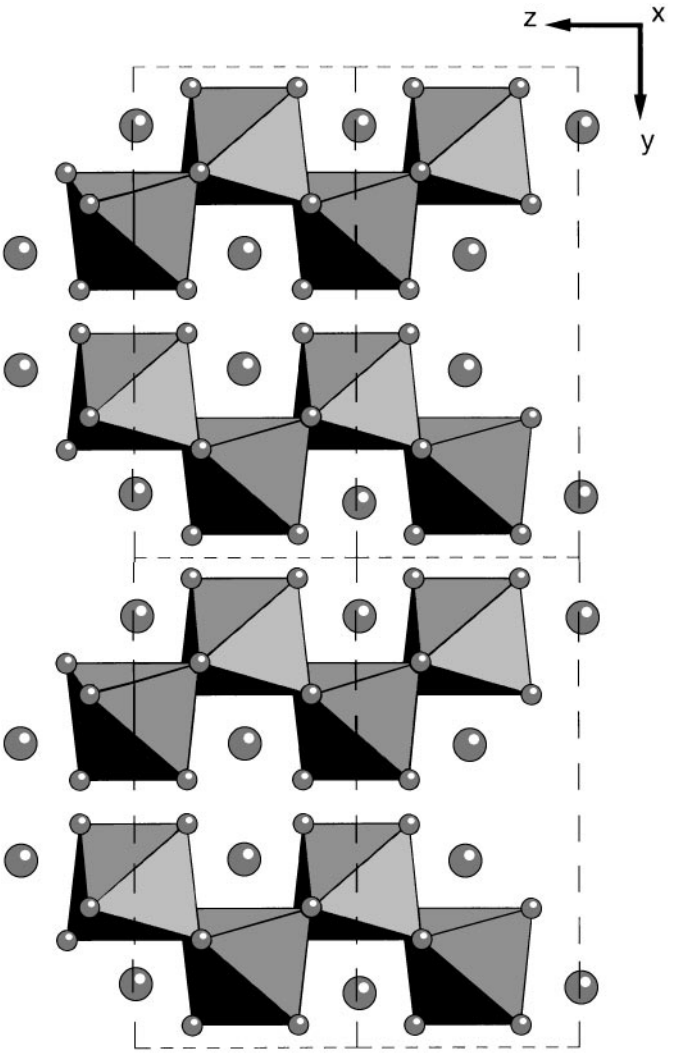

FIG. 1. Schematic semi-polyhedral representation of $Ce^{III}NbO_4$ along [100] showing strings of edge-sharing distorted NbO_6 octahedra. The Ce atoms, shown as spheres, are in approximately cubic eight-coordinate environment.

superstructure reflections in the **a*c*** plane of the fergusonite subcell while maintaining a common b axis (5). For $x \approx 0.08$ they reported a resultant unit cell of $a = 28.33$ Å, $b = 11.50$ Å, $c = 28.61$ Å, $\beta = 91.4°$ and for $x = 0.25$, $a = 29.54$ Å, $b = 11.41$ Å, $c = 12.39$ Å, $\beta = 99.3°$, both with space group $I2$.

While these authors (5) were able to prepare $x = 0.33$ as a single phase powder, the kinetics of oxidation prevented them from obtaining single crystals. No unit cell was reported for the $x = 0.33$ phase and consequently no structural relationship was deduced.

Electron diffraction in the transmission electron microscope (TEM) is a characterization technique which is well suited for the determination of unit cells and space group symmetry of crystalline solids, particularly when used in conjunction with careful XRD analysis. The previous authors left unanswered a number of questions about the structural relationships between the various subject phases, particularly for the $x = 0.33$ phase. Also, with recent advances in modulated structure concepts it is useful to review the $x \approx 0.08$ and 0.25 phases to redescribe them in terms of modulated variants of the underlying fergusonite structure.

The principal aim of this work is to provide a unified modulated structure description of the subject phases, to provide a summary of the various earlier reports, and to discuss the location of possible interstitial oxygen sites in the parent $CeNbO_4$ structure.

SYNTHESIS AND DATA COLLECTION

$Ce^{III}NbO_4$ starting material was prepared from the component oxides CeO_2 (99.9% Koch–Light) and Nb_2O_5 (> 99.9% Koch–Light). Anhydrous powders were intimately mixed in a mortar and pestle, then pressed into pellets and annealed at 1500°C on platinum foil for 17 h, and then rapidly quenched to room temperature in liquid nitrogen. The process was repeated with the second annealing being at 1350°C for 19 h. Powder XRD confirmed that the product after the second annealing, a yellow-green-colored powder, was a single crystalline phase.

The oxidized phase $x \approx 0.08$ was prepared by heating $Ce^{III}NbO_4$ powder in air at 850°C for 15 min in an alumina crucible, cooling in the furnace at 675°C (duration ~15 min), holding at 675°C for a further 20 min, and then quenching to room temperature in air. Hereafter it is referred to as $x = 0.08$ but the uncertainty in its exact composition is still implied. The $x = 0.25$ specimen was prepared by heating $Ce^{III}NbO_4$ powder in air at 850°C for 16 h, then cooling in the furnace to 600°C, holding at that temperature for 2.5 h, and then quenching to room temperature in air. The specimen was reground then reheated at 600°C for a further 4 days. The $x = 0.33$ specimen was prepared by heating $Ce^{III}NbO_4$ powder in an oxygen atmosphere at 400°C for 64 h and then cooling in the furnace to room temperature. The specimen was reground then reheated at 340°C for a further 64 h, again cooling the specimen to room temperature under oxygen.

Following oxidation all three materials were dark green in color and in each case XRD confirmed that the product was almost single phase. Unit cells for each phase were refined from XRD data collected using a Guinier–Hägg camera ($\lambda = 1.5406$ Å) with Si (NBS#640) as an internal standard. XRD profiles shown in Figs. 2 and 3 were obtained by scanning Guinier–Hägg films recorded without a Si internal standard.

For TEM characterization finely ground specimens were dispersed onto holey carbon grids. Electron diffraction patterns (EDPs) for the three oxidized phases and $Ce^{III}NbO_4$

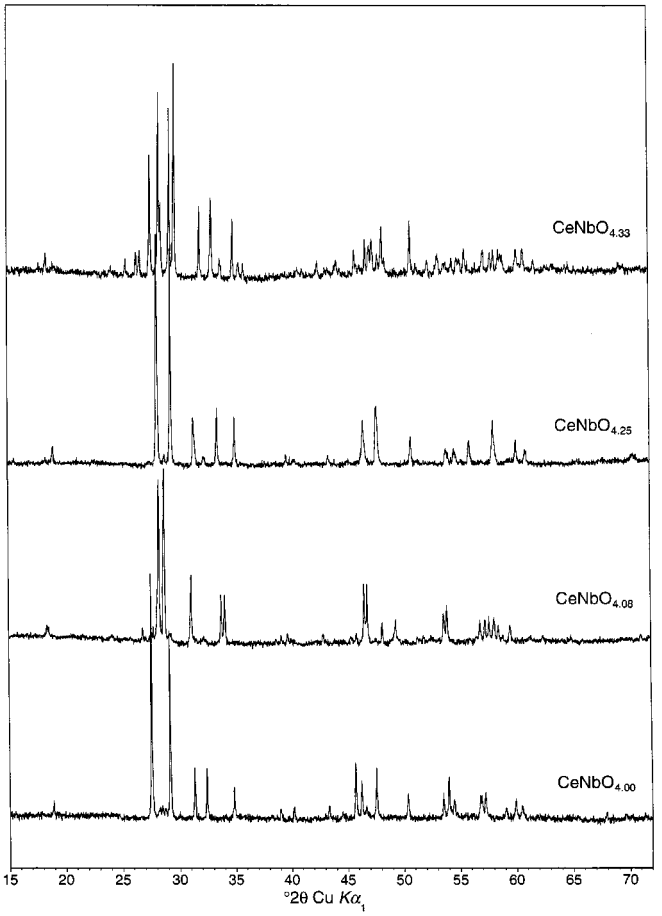

FIG. 2. X-ray powder diffraction profiles ($\lambda = 1.5406$ Å) between 15 and 72° 2θ for $Ce^{III}NbO_4$ and the three oxidized cerium niobate phases $CeNbO_{4+x}$ ($x = 0.08$, 0.25, and 0.33). Data were obtained by scanning XRD films obtained at room temperature using a Guinier–Hägg camera.

were obtained using Philips EM430, JEOL 100CX, and JEOL 2000EX TEMs.

RESULTS

X-ray Powder Diffraction

Figure 2 shows the XRD profiles between 15 and 72° 2θ for $Ce^{III}NbO_4$ and the three oxidized cerium niobate phases $CeNbO_{4+x}$ ($x = 0.08$, 0.25, and 0.33) juxtaposed. The broad similarities between the phases are apparent by comparison of the distribution of diffracted intensity as a function of 2θ. Refined unit cell dimensions for $Ce^{III}NbO_4$ and the subcells of the three oxidized phases are listed in Table 1 together with previously reported unit cells where available. Full listings of peak positions, relative intensities, and Miller indices are given in Tables 2–5. Note that the relative intensities are from samples relatively free of preferred orientation by virtue of the Guinier–Hägg data being a transmission experiment on a loosely packed specimen. By contrast, Bragg–Brentano data from such heavy X-ray absorbers are typically strongly affected by preferred orientation.

To illustrate the close relationship between the four phases the low-angle regions between 17 and 37° 2θ of the XRD profiles are expanded and shown in Fig. 3. All observed reflections have been indexed in terms of the parent subcell (refer to Table 1). The asterisked reflections in the profile of $CeNbO_{4.33}$ are satellite reflections. For the $CeNbO_{4.08}$ and $CeNbO_{4.25}$ phases weak satellites might also be observable and might account for some of the weak unassigned features, but due to the very high density of possible satellite reflections (see the next section) we have not attempted to index any of these features. The profile for $Ce^{III}NbO_4$ shows traces of $CeNbO_{4.08}$ due to a small amount of unavoidable oxidation during quenching and the profile for $CeNbO_{4.08}$ shows a trace of unoxidized $Ce^{III}NbO_4$.

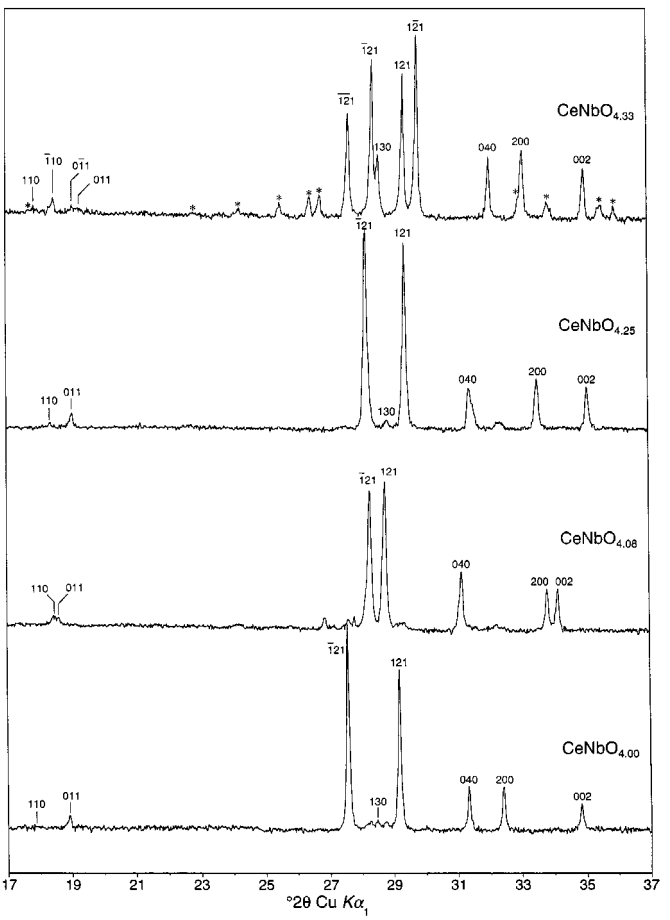

FIG. 3. Low-angle region between 17 and 37°2θ of the XRD profiles shown in Fig. 2 with all observed reflections indexed in terms of the parent subcell. The asterisked reflections in the profile of $CeNbO_{4.33}$ are satellite reflections. No satellite reflections were observable for the $CeNbO_{4.08}$ and $CeNbO_{4.25}$ phases.

TABLE 1
Refined Unit Cell Dimensions of $CeNbO_{4+x}$ Phases

Composition	Crystal system	Space group	a	b	c	α	β	γ	Unit cell volume
$CeNbO_{4.0}$	Monoclinic	$I2/a$	5.5342(2)	11.4016(6)	5.1583(3)	90.0	94.600(5)	90.0	324.43(2)
Ref. (1)			5.542(1)	11.414(1)	5.165(1)	90.0	94.60(1)	90.0	325.67(5)
				Parent Unit Cells					
$CeNbO_{4.08}$	Monoclinic	$I2/a$	5.3029(8)	11.483(2)	5.2515(8)	90.0	91.32(2)	90.0	319.70(6)
Ref. (5)			5.310	11.502	5.256	90.0	91.3	90.0	320.9
$CeNbO_{4.25}$	Monoclinic	$I2/a$	5.3522(8)	11.374(3)	5.116(1)	90.0	93.34(2)	90.0	310.95(8)
Ref. (5)			5.360	11.409	5.129	90.0	93.4	90.0	313.1
$CeNbO_{4.33}$[a]	Triclinic	$I1$	5.4374(8)	11.189(2)	5.1458(7)	90.56(1)	94.37(1)	88.19(1)	311.98(6)
				Resultant Unit Cells					
$CeNbO_{4.25}$[b]	Monoclinic	$P2_1/c$	14.371(2)	22.748(6)	11.820(2)	90.0	74.91(2)	90.0	3731(1)
$CeNbO_{4.33}$[c]	Triclinic	$P1$	6.721(1)	6.9021(9)	11.264(2)	99.12(1)	100.05(1)	110.50(1)	468.08(8)
Derived[d]			6.718(1)	6.901(1)	11.267(2)	99.15(1)	100.01(1)	110.48(1)	468.0(1)

[a] Refined using parent reflections only.
[b] Derived from parent unit cell dimensions ($\mathbf{a}_r = 2\mathbf{a}_p + 2\mathbf{c}_p$, $\mathbf{b}_r = 2\mathbf{b}_p$, $\mathbf{c}_r = -\mathbf{a}_p + 2\mathbf{c}_p$).
[c] Refined using all reflections.
[d] Derived from parent unit cell dimensions ($\mathbf{a}_r = \frac{1}{2}\mathbf{a}_p - \frac{1}{2}\mathbf{b}_p - \frac{1}{2}\mathbf{c}_p$, $\mathbf{b}_r = \frac{1}{2}\mathbf{a}_p + \frac{1}{2}\mathbf{b}_p - \frac{1}{2}\mathbf{c}_p$, $\mathbf{c}_r = \mathbf{a}_p + 2\mathbf{c}_p$).

TABLE 2
$CeNbO_{4.0}$ X-ray Powder Diffraction Data

h	k	l	I/I_0	d_{calc}	d_{obs}
0	1	1	6	4.687	4.687
−1	2	1	100	3.231	3.230
1	3	0	5	3.130	3.132
1	2	1	77	3.055	3.056
0	4	0	21	2.850	2.850
2	0	0	21	2.758	2.758
0	0	2	13	2.571	2.571
−1	1	2	2	2.353	2.350
−1	4	1	4	2.306	2.306
1	4	1	5	2.239	2.240
0	5	1	5	2.085	2.084
−1	3	2	3	2.032	2.033
2	4	0	23	1.982	1.982
−2	0	2	16	1.961	1.961
1	3	2	4	1.944	1.943
0	4	2	21	1.909	1.909
2	0	2	10	1.810	1.810
−1	6	1	11	1.710	1.710
−3	2	1	17	1.697	1.697
−2	5	1	3	1.690	1.690
1	6	1	8	1.682	1.682
3	2	1	10	1.619	1.620
−2	4	2	10	1.615	1.615
−1	2	3	11	1.607	1.607
1	7	0	4	1.562	1.562
−3	1	2	8	1.542	1.542
0	6	2	6	1.528	1.528
4	0	0	3	1.379	1.379

TABLE 3
$CeNbO_{4.08}$ X-ray Powder Diffraction Data

h	k	l_p	I/I_0	d_{calc}	d_{obs}
1	1	0	6	4.813	4.822
0	1	1	5	4.775	4.776
1	0	1	2	3.688	3.690
−1	2	1	94	3.154	3.156
1	3	0	—	3.103	3.105
1	2	1	100	3.103	3.105
0	4	0	40	2.871	2.872
2	0	0	28	2.651	2.651
0	0	2	28	2.625	2.625
−1	1	2	3	2.325	2.326
2	1	1	5	2.297	2.297
1	4	1	6	2.265	2.267
0	5	1	5	2.104	2.104
2	4	0	34	1.948	1.948
0	4	2	34	1.937	1.937
−2	0	2	11	1.887	1.885
2	0	2	14	1.844	1.845
−1	6	1	17	1.707	1.706
1	6	1	21	1.699	1.699
−3	2	1	11	1.618	1.618
−1	2	3	24	1.606	1.607
3	2	1	15	1.598	1.597
1	2	3	14	1.586	1.586
−2	4	2	9	1.577	1.577
0	7	1	4	1.566	1.566
2	4	2	9	1.552	1.551

TABLE 4
$CeNbO_{4.25}$ X-ray Powder Diffraction Data

h	k	l_p	I/I_0	d_{calc}	d_{obs}
1	1	0	2	4.836	4.833
0	1	1	7	4.660	4.660
−1	2	1	100	3.162	3.163
1	3	0	5	3.092	3.090
1	2	1	94	3.035	3.034
0	4	0	21	2.844	2.845
2	0	0	25	2.672	2.670
0	0	2	21	2.554	2.554
2	1	1	4	2.266	2.266
1	4	1	2	2.229	2.229
0	5	1	3	2.078	2.077
2	4	0	19	1.947	1.948
−2	0	2	26	1.902	1.902
2	0	2	12	1.795	1.795
−1	6	1	7	1.697	1.699
1	6	1	7	1.676	1.678
−3	2	1	10	1.640	1.641
3	2	1	19	1.586	1.586
1	2	3	10	1.536	1.536
2	4	2	6	1.518	1.518
4	0	0	3	1.336	1.334

TABLE 5
$CeNbO_{4.33}$ X-ray Powder Diffraction Data

h	k	l_r	h	k	l_p	I/I_0	d_{calc}	d_{obs}
0	−1	1				1	6.093	6.094
−1	1	0	0	2	0	1	5.594	5.599
−1	1	1				1	4.997	4.991
0	1	1	1	1	0	4	4.937	4.936
1	0	1	−1	1	0	8	4.818	4.816
0	−1	2	0	−1	1	4	4.675	4.673
−1	0	2	0	1	1	2	4.651	4.651
−1	1	2				2	3.911	3.911
0	1	2				4	3.678	3.677
0	−1	3				9	3.496	3.497
−1	2	0				11	3.376	3.376
1	−2	1				12	3.336	3.336
0	−2	1	−1	−2	1	57	3.228	3.229
−2	0	1	−1	2	1	86	3.146	3.148
−1	2	1	1	3	0	35	3.118	3.122
−1	−1	3				2	3.067	3.069
−1	1	3	1	2	1	79	3.044	3.044
1	−1	3	1	−2	1	100	3.000	3.002
−2	2	0	0	4	0	34	2.797	2.796
0	−1	4				9	2.721	2.722
1	1	2	2	0	0	37	2.709	2.709
2	−1	2				9	2.644	2.644
−1	−1	4	0	0	2	28	2.565	2.565
−1	−2	1				8	2.533	2.531
−1	−2	2				7	2.499	2.500
0	1	4	2	1	1	1	2.286	2.286
−1	0	5	1	1	2	4	2.211	2.211
2	−2	3				4	2.190	2.189
−3	2	0				7	2.124	2.122
−2	3	1	1	5	0	4	2.091	2.091
1	−3	3				4	2.080	2.080
2	−3	2	0	−5	1	5	2.056	2.055
−3	2	2	0	5	1	7	2.046	2.045
0	−3	3	−1	−3	2	3	2.031	2.031
−1	3	2	2	4	0	12	1.977	1.977
0	3	1				5	1.969	1.969
−2	3	2				4	1.959	1.959
2	−1	4				4	1.951	1.953
−2	−2	2	−2	0	2	17	1.938	1.938
1	−2	5	1	−3	2	14	1.922	1.924
3	−1	2	−2	4	0	17	1.916	1.917
1	−3	4	0	−4	2	9	1.897	1.897
−3	1	4	0	4	2	22	1.884	1.884
0	0	6	2	0	2	24	1.795	1.795
1	3	0				4	1.779	1.779
2	2	1	−3	0	1	7	1.746	1.746
0	−3	5				4	1.720	1.719
−1	1	6	2	2	2	9	1.718	1.717
1	−1	6	2	−2	2	5	1.702	1.703
−3	−1	4	−1	−6	1	5	1.697	1.697
1	3	1	−3	−2	1	7	1.682	1.682
1	−2	6				1	1.669	1.669
−3	3	3	1	6	1	7	1.666	1.665
−4	2	1	−1	6	1	6	1.663	1.661
3	1	1	−3	2	1	11	1.651	1.651
3	−3	3	1	−6	1	5	1.644	1.644
0	1	6				4	1.627	1.626
3	0	3	−3	3	0	9	1.606	1.607
−3	−1	5	−1	2	3	8	1.591	1.591

Electron Diffraction

Figure 4 shows $[010]_p$ zone axis EDPs of the (a) $x = 0$, (b) $x = 0.08$, (c) $x = 0.25$, and (d) $x = 0.33$ phases. The same strongly scattering pseudo-tetragonal array of parent substructure reflections (indexed in (a)) are visible in all four EDPs. In the case of the oxidized phases, however, additional satellite reflections are also present. Note the change in orientation of the rows of satellite reflections as x increases as well as the growth in intensity of the satellite reflections relative to the parent subcell reflections.

The most complex phase crystallographically is the incommensurately modulated $x = 0.08$ phase in which rows of satellite reflections can be seen to run along the $\sim[10, 0, 4]_p^*$ and $[\bar{4}, 0, 10]_p^*$ directions of reciprocal space (compare Fig. 4b with Fig. 4a). The basis vectors defining the pseudo-tetragonal square mesh of satellite reflections surrounding each strong parent reflection in Fig. 4b are labeled $\mathbf{q}_1$ and $2\mathbf{q}_2$, respectively (see Fig. 5a). (The reason for labeling $2\mathbf{q}_2$ as $2\mathbf{q}_2$ and not $1\mathbf{q}_2$ can be see in the $\mathbf{q}_2 - \mathbf{b}^*$ section of reciprocal space shown in Fig. 5b, in which it is apparent that satellite reflections of the form $\mathbf{b}_p^* + 1\mathbf{q}_2$ exist. Note that the parent structure is body-centered $I12/a1$ so that $\mathbf{b}_p^*$ is not an allowed parent substructure reflection. The $\mathbf{G}_p \pm 2\mathbf{q}_2$ satellite reflections apparent in Figs. 4b and 5 are thus second harmonic satellite reflections.) Note that $5\mathbf{q}_1 - 4\mathbf{q}_2$ is very close to $2\mathbf{a}_p^*$ while $2\mathbf{q}_1 + 10\mathbf{q}_2$ is very close to $2\mathbf{c}_p^*$, thus implying that $\mathbf{q}_1 \sim \frac{1}{29}[10, 0, 4]_p^*$ and $2\mathbf{q}_2 \sim \frac{1}{29}[\bar{4}, 0, 10]_p^*$.

TABLE 5—*Continued*

h	k	l_r	h	k	l_p	I/I_0	d_{calc}	d_{obs}
0	−4	3	1	−5	2	9	1.583	1.583
−4	0	2	−2	4	2	10	1.573	1.572
1	−4	4				6	1.567	1.567
−4	0	1				6	1.564	1.565
0	−2	7	1	−2	3	10	1.534	1.535
3	−4	2	0	−7	1	3	1.529	1.529
−2	2	6	2	4	2	10	1.522	1.521
2	−2	6	2	−4	2	5	1.500	1.500
2	3	0				2	1.478	1.478
−4	3	3				3	1.466	1.467
4	−3	2				2	1.462	1.461
0	−4	5	−1	−4	3	3	1.443	1.443
−1	−4	3				4	1.437	1.437
−4	−1	1	−3	3	2	2	1.403	1.402

Indexation of the (a) $[010]_p$ and (b) $\sim[502]_p$ zone axis EDPs of Fig. 5 is thus with respect to the set of five linearly independent basis vectors given by $M^* = \{\mathbf{a}_p^*, \mathbf{b}_p^*, \mathbf{c}_p^*, \mathbf{q}_1, \mathbf{q}_2\}$. The observed extinction conditions characteristic of this complex incommensurately modulated phase when indexed with respect to the above basis vectors are as follows: $F(hklmn) = 0$ unless $h + k + l$ is even (requiring a body-centered parent substructure), $F(h0lmn) = 0$ unless h and l are both even (requiring the parent substructure to have an a glide perpendicular to $\mathbf{b}_p$: the satellite reflections do not occur around the a glide forbidden parent substructure reflections in $[010]_p$ zone axis EDPs) and $F(hklmn) = 0$ unless $k + n$ is even (a centering condition corresponding to the fact that $\mathbf{q}_1$ and $(\mathbf{b}_p^* + \mathbf{q}_2)$ are the real primitive primary modulation wavevectors). The corresponding implied superspace symmetry operations (see, for example , Refs. (7,

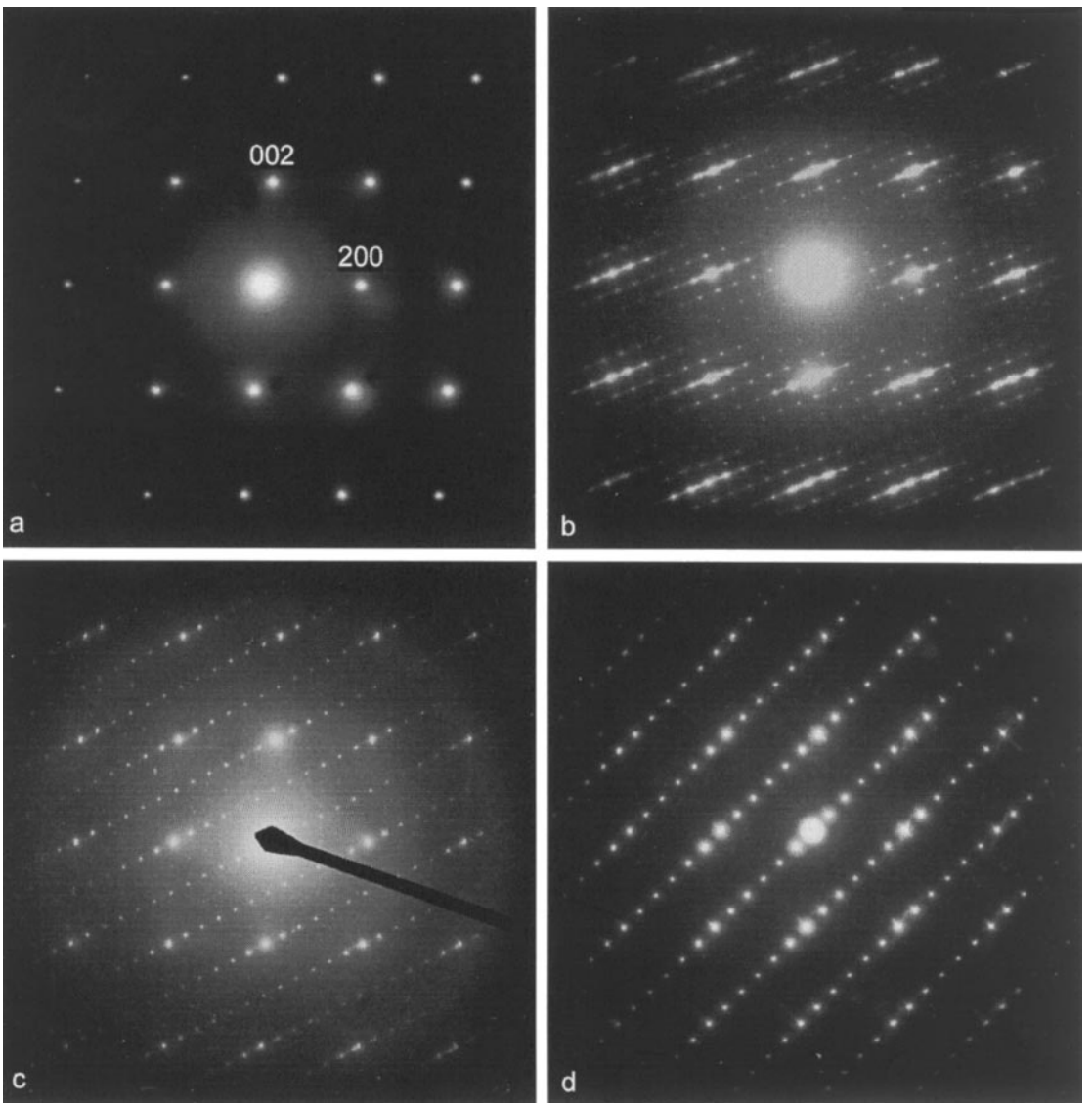

FIG. 4. $[010]_p$ zone axis EDPs of the (a) $x = 0$, (b) $x = 0.08$, (c) $x = 0.25$, and (d) $x = 0.33$ phases. Note the same strongly scattering pseudo-tetragonal array of parent substructure reflections (indexed in (a)) visible in all four EDPs.

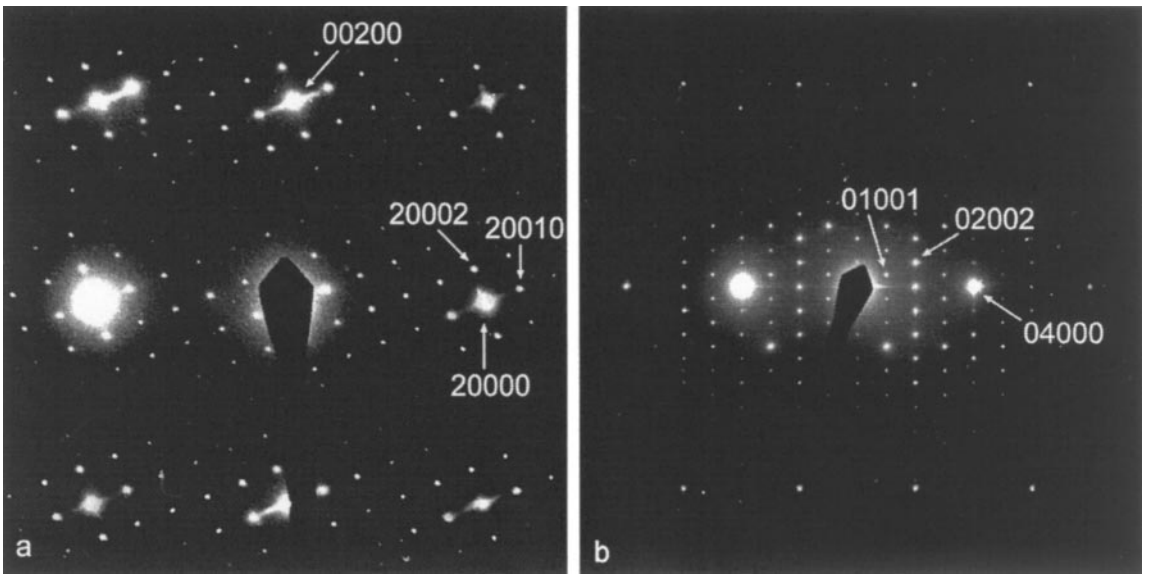

FIG. 5. EDPs of the $x = 0.08$ phase along the (a) $[010]_p$ and (b) $\sim[502]_p$ zone axes. Indexation is with respect to the set of five linearly independent basis vectors given by $M^* = \{\mathbf{a}_p^*, \mathbf{b}_p^*, \mathbf{c}_p^*, \mathbf{q}_1, \mathbf{q}_2\}$.

(8)) are $\{x_1 + \frac{1}{2}, x_2 + \frac{1}{2}, x_3 + \frac{1}{2}, x_4, x_5\}$, $\{x_1 + \frac{1}{2}, -x_2, x_3, x_4, x_5\}$, and $\{x_1, x_2 + \frac{1}{2}, x_3, x_4, x_5 + \frac{1}{2}\}$, respectively. These superspace symmetry operations, in conjunction with the assumed superspace inversion operation $\{-x_1, -x_2, -x_3, -x_4, -x_5\}$, can be taken to be the generators of the overall superspace group.

In the case of the $x = 0.25$ superstructure phase, the resultant reciprocal space unit cell is given by $\mathbf{a}_r^* = \frac{1}{12}[402]_p^*$, $\mathbf{b}_r^* = \frac{1}{4}[020]_p^*$, and $\mathbf{c}_r^* = \frac{1}{3}[\bar{1}01]_p^*$. (The corresponding relationship in real space is given by $\mathbf{a}_r = 2\mathbf{a}_p + 2\mathbf{c}_p$, $\mathbf{b}_r = 2\mathbf{b}_p$, and $\mathbf{c}_r = -\mathbf{a}_p + 2\mathbf{c}_p$: r for resultant.) Thus 12 $\mathbf{a}_r^* = [402]_p^*$ while $6\mathbf{c}_r^* = [\bar{2}02]_p^*$, as is apparent from a comparison of Figs. 4a and 4c. The doubling of the parent b axis dimension is necessitated by the $1/2\mathbf{b}_p^*$ height of the first order Laue zone (FOLZ) ring above the zero order Laue zone (ZOLZ) reflections in the $[010]_p$ zone axis EDP of Fig. 6a as well as by the $[10\bar{1}]_r$ or $[100]_p$ zone axis EDP of Fig. 6b. That the resultant cell is primitive is clear from Figs. 4c and 6. The existence of a c glide perpendicular to the resultant b axis is apparent from the absence of

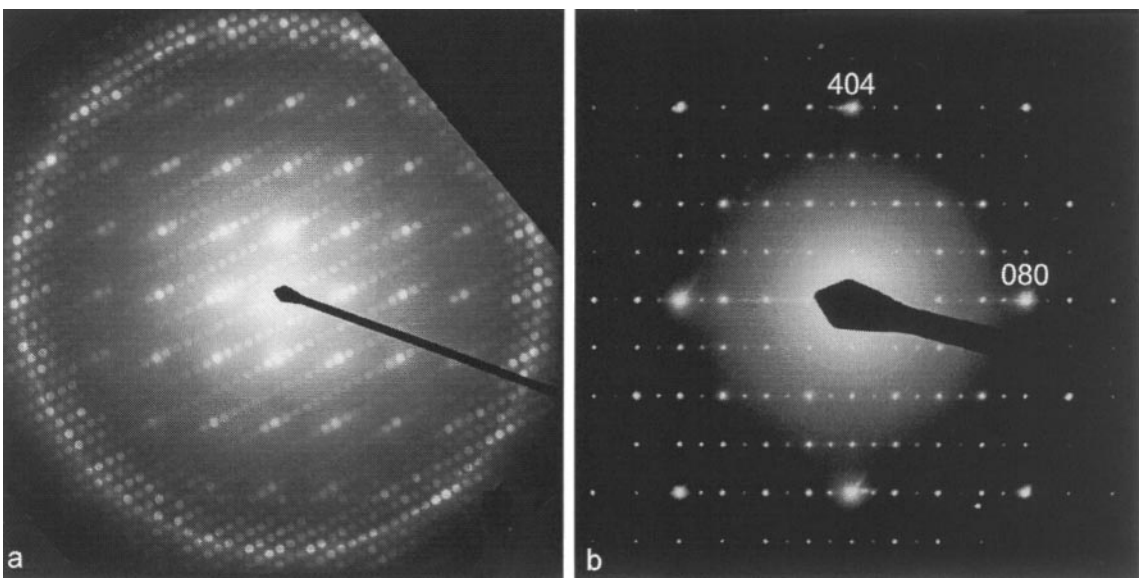

FIG. 6. (a) $[010]_p$ and (b) $[10\bar{1}]_r$ or $[100]_p$ zone axis EDPs for the $x = 0.25$ phase. Indexation in (b) is with respect to the resultant supercell.

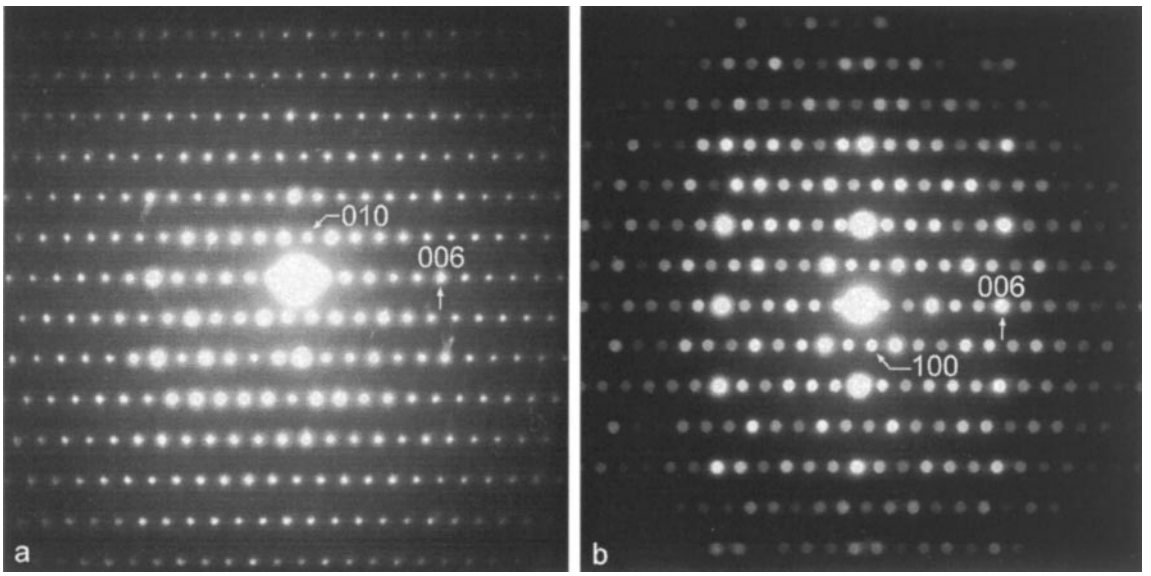

FIG. 7. (a) $[100]_r$ and (b) $[010]_r$ zone axis EDPs for the $x = 0.33$ phase. Indexation is with respect to the resultant supercell.

alternate rows of satellite reflections in the ZOLZ and the consequent doubled density of reflections in the FOLZ relative to the ZOLZ apparent in the $[020]_p = [010]_r$ zone axis microdiffraction pattern of Fig. 6a. The minimum resultant space group symmetry is thus $P1c1$. The only possible space group symmetries for the resultant phase are thus $P1c1$, $P12/c1$, or $P12_1/c1$, with the latter perhaps the most likely.

Finally, in the case of the triclinic $x = 0.33$ superstructure phase, the resultant reciprocal space unit cell is given by $\mathbf{a}_r^* = \frac{1}{3}[2\bar{3}\bar{1}]_p^* = [1\bar{1}0]_p^* - \frac{1}{3}[101]_p^*$, $\mathbf{b}_r^* = \frac{1}{3}[23\bar{1}]_p^* = [110]_p^* - \frac{1}{3}[101]_p^*$, and $\mathbf{c}_r^* = \frac{1}{3}[101]_p^*$ (see the $[100]_r$ and $[010]_r$ zone axis EDPs shown in Figs. 7a and 7b, respectively, and the $[1\bar{1}0]_r$ zone axis EDP of Fig. 4d). Note that all resultant reflections can thus be expressed in the form $\mathbf{G}_p \pm \frac{1}{3}[101]_p^*$. In this sense, the triclinic phase is the simplest of all three of the modulated phases. (The corresponding relationship in real space is given by $\mathbf{a}_r = \frac{1}{2}\mathbf{a}_p - \frac{1}{2}\mathbf{b}_p - \frac{1}{2}\mathbf{c}_p$, $\mathbf{b}_r = \frac{1}{2}\mathbf{a}_p + \frac{1}{2}\mathbf{b}_p - \frac{1}{2}\mathbf{c}_p$, $\mathbf{c}_r = \mathbf{a}_p + 2\mathbf{c}_p$.)

DISCUSSION

The crystal structures of the series of phases obtained when $Ce^{III}NbO_4$ is heated in air or oxygen are very closely related to each other and the reduced starting material. This is evident by inspection of the XRD profiles (Fig. 2) and from the similarity in unit cell dimensions of the parent subcell (Table 1). The difference between XRD profiles is principally in the peak positions for corresponding subcell reflections (Fig. 3) associated with variable distortion of the subcell.

The structural differences necessarily arise from the arrangement of additional oxygen atoms, which Ce^{III} atoms are oxidized to Ce^{IV}, and how each structure relaxes to satisfy the new chemical bonding requirements and nonbonding interactions. Because the XRD profiles are dominated by scattering from the metal atoms it is not surprising that the relative intensities of diffraction peaks remain much the same.

Upon oxidation of $Ce^{III}NbO_4$ there is a volume decrease: 1.5% for $x = 0.08$, 4.2% for $x = 0.25$, and 3.8% for $x = 0.33$. This can be understood by considering the bond-length bond-valence relationship (9, 10). For an idealized eight-coordinate polyhedron, CeO_8, oxidation from Ce^{III} to Ce^{IV} would lead to $\sim$9% shortening of bonds, from 2.51 to 2.28 Å. If an additional oxygen atom is simultaneously added, i.e., the coordination increases from $Ce^{III}O_8$ to $Ce^{IV}O_9$, then the shortening is only $\sim$7%, from 2.51 to 2.33 Å. In other words, despite the need to accommodate additional oxygen atoms, the oxidation of some of the Ce^{III} atoms to Ce^{IV} will tend to pull the structure together more tightly. Charge balance requires $\sim\frac{1}{6}$ of the Ce^{III} to be oxidized for $x = 0.08$, $\frac{1}{2}$ for $x = 0.25$, and $\sim\frac{2}{3}$ for $x = 0.33$.

As stated earlier, the modulation of the underlying $Ce^{III}NbO_4$ parent is necessarily due to ordering of interstitial oxygens and Ce^{IV} atoms and associated atomic displacements to satisfy nonbonded O–O distances as well as bonding requirements for metals and oxygens. The modulation wave vectors for the three oxidized phases, as determined by electron diffraction, appear to show continuous variation in magnitude and direction with increasing oxidation (Fig. 4). The similarity between these phases in diffraction space is best seen by comparison of related modulation wave vectors (Fig. 8). This similarity is obscured in real space. There is no obvious relationship between the resultant unit cells for the two commensurately modulated

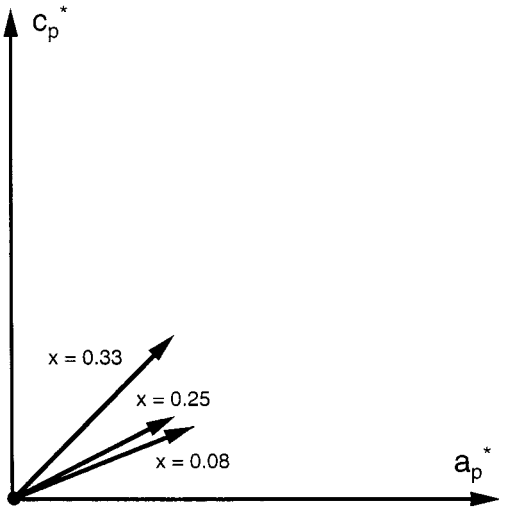

FIG. 8. Related modulation wave vectors for $x = 0.08$ ($\mathbf{q}_1 = \frac{1}{29}[10, 0, 4]^*_p$), $x = 0.25$ ($\mathbf{a}^*_r = \frac{1}{12}[402]^*_p$), and $x = 0.33$ ($c^*_r = \frac{1}{3}[101]^*_p$) plotted as vectors in the **a*c*** plane of an idealized parent reciprocal lattice. The three wave vectors, all with similar magnitudes, vary in direction with increasing oxygen content. For the $x = 0.08$ and 0.25 phases there are additional wave vectors to these.

phases, $x = 0.25$ and 0.33 (see Table 1), and there is no true resultant unit cell for the incommensurately modulated phase, $x = 0.08$. The advantages of a modulated structure description of this series of phases, and the incommensurate $x = 0.8$ phase in particular, were acknowledged by previous authors (11) but they did not present such a description.

While it is beyond the scope of this present study to solve and refine the structures of the oxidized phases, it is possible to identify the most likely site for the interstitial oxygens. As observed by previous authors (1), fergusonite-type is monoclinically distorted scheelite-type, which in turn can be considered a distorted superstructure of fluorite-type. In fluorite-type $Fm\bar{3}m$ (12) there are two cubic (eight-coordinate) sites: the 4*a* site, which is occupied by the metal atom, and the 4*b* site, which is empty. Additional oxygen could be accommodated in the vicinity of this empty site if its bonding requirements could be satisfied and nonbonded O–O distances made large enough.

The corresponding position to this empty eight-coordinate fluorite-type site in $Ce^{III}NbO_4$ occurs at $\frac{1}{4}, \frac{1}{8}, \frac{1}{2}$ in the setting of the published structure (1). An interstitial oxygen at this position has a shortest O–O distance of 2.02 Å. Displacing the interstitial oxygen to $\frac{1}{4}$, 0.10, $\frac{1}{2}$ maximises the shortest distance to 2.19 Å, without displacing any other atoms. This site is adjacent to two Ce atoms at 2.59 Å.

Figure 9 shows a schematic semi-polyhedral representation of the structure $Ce^{III}NbO_4$with the darker small spheres representing the proposed interstitial oxygen sites. The 8 + 2 coordination environment of the Ce atoms is illustrated. Relatively small (0.1–0.2 Å) local displacements of atoms in this model would be sufficient to allow for bonding and nonbonding distances to be optimized. Such small displacements of atoms, particularly of the metal atoms, would leave the XRD pattern relatively unchanged, as is observed.

Like $Ce^{III}NbO_4$, $Ce^{III}TaO_4$ can be oxidized progressively to give a series of oxidized phases, the main difference being that $Ce^{III}TaO_4$ has a different parent structure, namely the low-temperature $LaTaO_4$-type structure (1). In a recent structural study of $CeTaO_{4+x}$ ($x \approx 0.17$) using XRD data (13), in which two-thirds of the Ce^{III} atoms are oxidized, it was deduced that the Ce atoms adjacent to the interstitial oxygen were not oxidized. This is also likely for the present fergusonite-type cerium niobate oxidized phases, due to the fact that interstitial oxygens can be accommodated more easily in a Ce^{III} coordination sphere as a mean Ce^{III}–O distance of 2.56 Å for $Ce^{III}O_9$ would minimize O–O crowding.

CONCLUSION

The most striking chemical feature of the subject cerium niobate phases is the relatively mild conditions under which they are progressively oxidized from one structure to another. This is consistent with the diffusion of oxygen into $Ce^{III}NbO_4$ with minimal bond breaking. At the very least

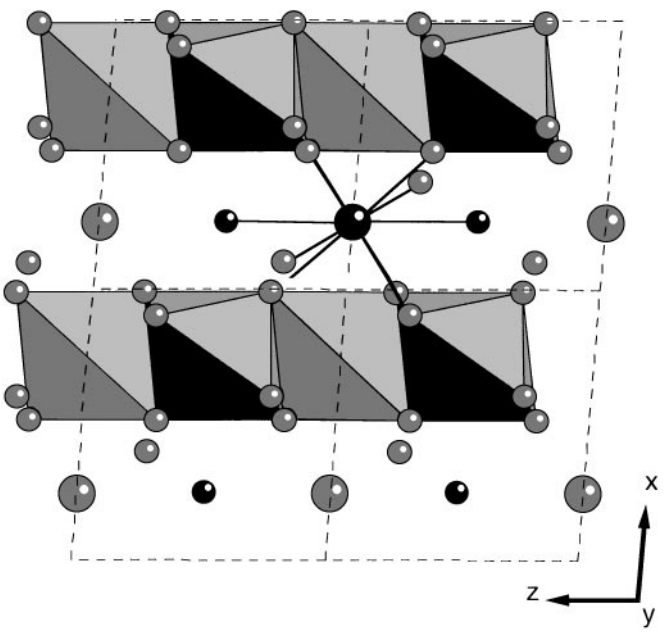

FIG. 9. Schematic semi-polyhedral representation of $Ce^{III}NbO_4$ as in Fig. 1, but along [001] and showing the location of the most likely site(s) for additional oxygen atoms (smaller dark spheres) in the oxidized phases. The 8 + 2 coordination environment of the Ce atoms is illustrated.

the XRD intensities confirm that the metal atom array remains unchanged, apart from the small variation in the monoclinic distortion. As the fergusonite structure type can be related to fluorite-type the oxygen ion conductivity of cubic stabilized zirconias and chemically substituted cerias springs to mind. In these analogous phases there is precedent for high mobility of the anions at relatively low temperatures while preserving the cation array.

The stoichiometry of the three modulated structures ($x = 0.08$, 0.25, and 0.33) requires that they differ in their interstitial oxygen atom and Ce^{III}/Ce^{IV} ordering. While the periodicity of this ordering is given by the modulation wave vectors presented here it is still necessary to obtain high-resolution neutron powder diffraction for these phases to be able to solve and refine these structures. XRD data show that the differences between the structures must be predominantly in the occupancy of the interstitial oxygen sites and associated relaxation of the surrounding oxygen array. Therefore, neutron diffraction data are required as the metal and oxygen atoms have similar scattering lengths, whereas for XRD the scattering is dominated by the metal atoms whose positions remain relatively unchanged.

REFERENCES

1. A. Santoro, M. Marezio, R. S. Roth, and D. Minor, *J. Solid State Chem.* **35,** 167 (1980).
2. K. A. Gingerich and H. E. Bair, *Adv. X-ray Anal.* **7,** 22 (1964).
3. T. Negas, R. S. Roth, C. L. McDaniel, H. S. Parker, and C. D. Olson, *Mater. Res. Bull.* **12,** 1161 (1977).
4. R. S. Roth, T. Negas, H. S. Parker, D. B. Minor, and C. Jones, *Mater. Res. Bull.* **12,** 1173 (1977).
5. R. S. Roth, T. Negas, H. S. Parker, D. B. Minor, C. D. Olson, and C. Skarda, *in* "The Rare Earths in Modern Science and Technology" (Proc. of the 13th Rare Earth Res. Conf.; G. J. McCarthy and J. J. Rhyne, Eds.), pp. 163–171. Plenum, New York, 1978.
6. R. J. Cava, T. Negas, R. S. Roth, H. S. Parker, D. B. Minor, and C. D. Olson, *in* "The Rare Earths in Modern Science and Technology" (Proc. of the 13th Rare Earth Res. Conf.; G. J. McCarthy and J. J. Rhyne, Eds.), pp. 181–187. Plenum, New York, 1978.
7. S. van Smaalen, *Crystallogr. Rev.* **4,** 79 (1995).
8. R. L. Withers, S. Schmid, and J. G. Thompson, *Prog. Solid State Chem.* **26,** 1 (1998).
9. I. D. Brown and D. Altermatt, *Acta Crystallogr. Sect. B* **41,** 244 (1985).
10. N. E. Brese and M. O'Keeffe, *Acta Crystallogr. Sect. B* **47,** 192 (1991).
11. R. J. Cava and R. S. Roth, *AIP Conf. Proc.* **53,** 361 (1979).
12. A. J. C. Wilson, Ed., "International Tables for Crystallography," Vol. C. Kluwer Academic, Dordrecht, 1992.
13. J. G. Thompson, A. D. Rae, N. Bliznyuk, and R. L. Withers, *J. Solid State Chem.*, in press.